2 PF Ring

2-1 Operation Summary

The timetable of the PF ring and PF-AR operations in FY2009 is shown in Fig. 1. The operations of both rings were mostly conducted as per the schedule.

The operation statistics of the PF ring are summarized in Table 1. The statistics for each fiscal year since the commencement of the operation are shown in Fig. 2. The total operation time was recovered after the straight-section upgrade project in 2005, amounting to more than 5000 h for each of the past three years. However, the operation time has been gradually decreasing with each passing year because of the reduction of the operation budget. In FY2009, the scheduled user time and the actual user time excluding the time losses due to machine troubles were 4032.0 h and 3943.6 h, respectively. The ratio of the actual user time to the scheduled time has been maintained over 99%. The failure rate, which is the ratio of the failure time to the total operation time, is shown in Figure 3. The rf systems experienced troubles twice: One was a failure in a klystron and the other was a failure in the high-voltage power supply. Owing to these troubles, the operation was conducted with three rf cavities (instead of four cavities as is the norm), because of which the stored current was limited to 430 mA (which is otherwise normally 450 mA). Since the klystron had been used for over 50000 h, it was renewed during the summer shutdown. The power supply had been employed for over 20 years. Thus, it is planned to be renewed during the summer shutdown of 2010.

In FY2009, the user operation with a continuous injection, referred to as a "top-up injection," was carried out owing to the fact that a simultaneous injection to the three rings (PF ring, KEKB LER, and KEKB HER) had been achieved. The beam current was usually maintained at 450.0 ± 0.1 mA, which corresponds to a current accuracy of $\pm 1 \times 10^{-4}$ with an injection repetition frequency of 0.5 Hz. The operation in the single-bunch mode was conducted at a beam current of 50.0 ± 0.1 mA for 3 weeks. The 3-GeV operation was carried out without the continuous injection for 1 week because a full-energy injection has not been realized yet. However, the 3-GeV operation was terminated because of several reasons at the end of FY2009.

Table 1 Operation statistics of PF ring in FY2009.

	Total
Ring Operation Time (hours)	4976.0
Scheduled user time (hours)	4008.0
Actual user time T (hours)	3965.3
Failure time (hours)	42.7

Timetable of the Machine Operation in FY 2009

PF: PF ring

AR: PF-AR

Color	Description	Color	Description
Red	Tuning and ring machine study	Green	Short maintenance and /or machine study
Yellow	Ring machine study	Purple	Experiment using SR
Dark blue	Single bunch operation at 2.5 GeV	Light blue	Multi bunch operation at 3.0 GeV (the last operation)

Figure 1
Timetable of machine operation in FY2009.
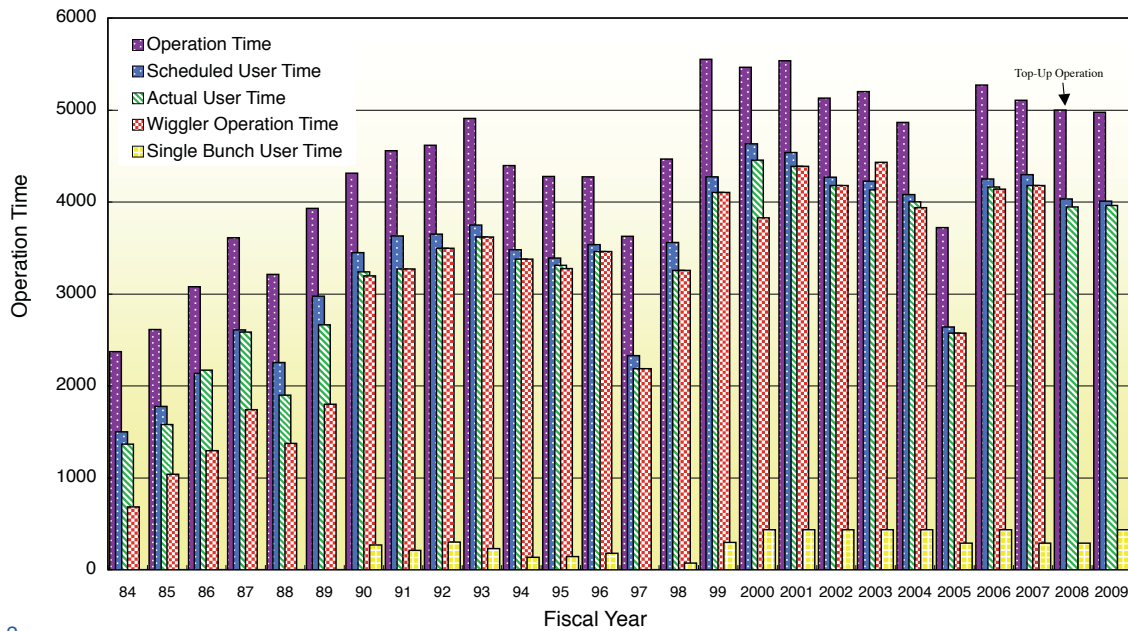
Figure 2
Total operation time, scheduled user time, actual user time, wiggler operation time, and single-bunch user time in each fiscal year since the commencement of the operation.
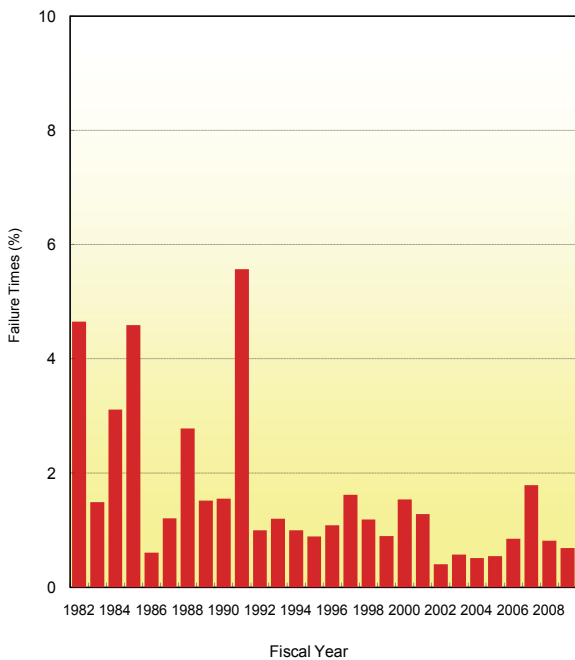
Figure 3
Failure rate of PF ring, which is the ratio of the failure time to the total operation time.

2-2 Top-Up Injection

To achieve top-up injection for the PF-Ring, many difficulties had to be overcome, the most severe of which was the upgrade of the injector linac. The KEK linac is a 600-m long injector for four storage rings in different energy and particles: PF-Ring (2.5 GeV; e⁻), PF-AR (3.0 GeV; e⁻), KEKB HER (8 GeV; e⁻) and LER (3.5 GeV; e⁺). Some of the major upgrades made in recent years are listed below. (Details of each topic have already been reported in previous PF activity reports.)

2004: Injector upgrade
• Construction of new beam transport line at the end of linac (DC Bend)
• Study on nonlinear effects of sextupole magnet in side the kicker bump
• Development of pulsed quadrupole magnet for injection (at PF-AR)
2006: Injector upgrade
• Development of pulsed bending magnet
• Study on radiation safety regulation for top-up
• Injection with common lattice for PF (2.5 GeV) and KEKB-HER (8 GeV)
2007: Injector upgrade
• Installation of pulsed bending magnet
• New positron target with hole (for KEKB LER) wo slit in the beam transport line
• New beam dump downstream of PF-BT
• Development pulsed sextupole magnet
2008: Injector upgrade:
•Linac timing system upgrade
•Simultaneous injection to KEKB HER, LER, PF-Ring
• Installation/injection with pulsed sextupole magnet
• Top-up injection during single-bunch operation

After these many efforts to establish a stable top-up injection, full-time top-up operation started in April 2009. Figure 4 shows the weekly history of beam current. The stored current was maintained at 430 mA, slightly less than the normal value of 450 mA, because one of the four RF cavities was suspended due to a high voltage power supply trouble. There are two beam current decreases at 10:00 and 22:00 every day; these are scheduled interruptions due to the injection to PF-AR, which takes 10 to 15 minutes and results in a 3 to 5 mA decrease in the beam current. The other current dip
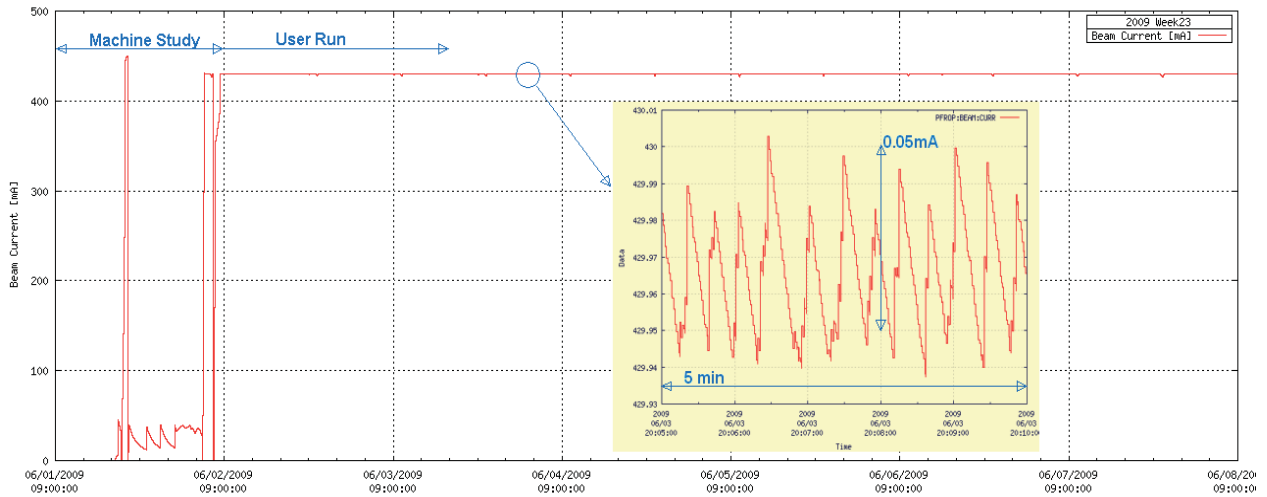
Figure 4
Beam current history for 1 week. A circle in the figure shows the details of the top-up injection for 5 minutes.

was caused by the sudden shutdown of the RF klystron of the injector linac.

An example of the beam current record for 5 minutes is also shown in the figure. Variation in the beam current is 0.5 to 1 mA, which corresponds to almost 0.01 to 0.02% of the stored current.

Currently, we are using four kicker magnets for injection. We plan to use a pulsed sextupole magnet during user operation in 2010.

2-3 Feedback

The suppression of various kinds of beam instability is essential to produce stable and intense synchrotron radiation for users' experiments. In the KEK-PF, both transverse and longitudinal bunch-by-bunch feedback systems have been developed together with SPring-8 and KEK B-Factory [1-3]. We have been using two kinds of digital signal processor: an "iGp system" [4] for the longitudinal plane, and a "SPring-8 signal processor" [5] for the transverse plane. Both systems have been running without any serious failure for years. In 2009, we decided to use the iGp system for both transverse and longitudinal plane in order to simplify the whole system and to reduce the future cost of development and maintenance load.

Figure 5 shows a block diagram of the transverse feedback system. The analog front-end part has been modified to match the iGp, while the power amplifier and stripline kickers are kept the same as the SPring-8 system. The iGp box is composed of a 1 Gigasample ADC, FPGA (Field Programmable Gate Array) signal processor, and DAC. The FPGA functions as a 16-Tap FIR filter designed to have maximum gain at a betatron frequency and to produce a 90-degree phase shift to

damp the unstable beam motion.

Figures 6(a) and 2(b) show the transverse beam profile measured by CCD camera for the open- and closed-loop conditions, respectively. We can see that the horizontal beam size is reduced and peak intensity is enhanced by approximately 20% by closing the feedback loop. The feedback system based on iGp has shown sufficient performance to suppress the transverse instability caused by the ion-related effect in the PF-Ring, and the system helps to shorten the damping time of coherent beam oscillation during the beam injection, which is induced by imperfections of the injection kicker bump.
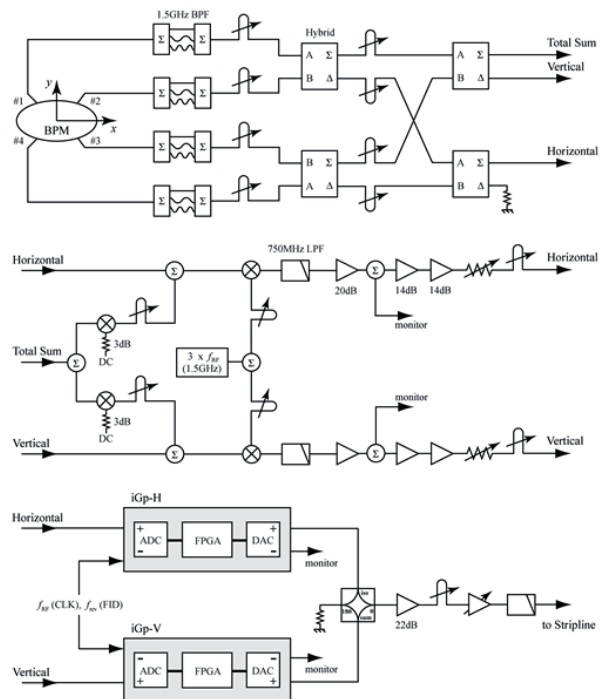
Figure 5
Block diagram of transverse bunch-by-bunch feedback system. The gray box shows the digital signal processor iGp.
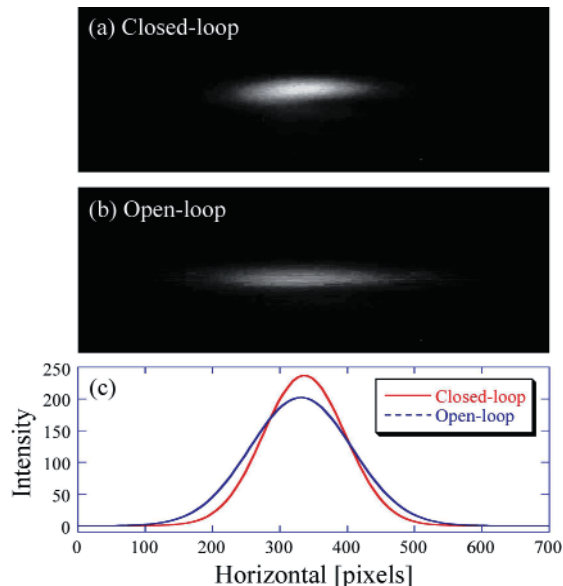
Figure 6
Transverse beam profiles measured by a CCD camera when the feedback loop is closed (a) and open (b), respectively.

REFERENCES

[1] *Activity Report 2006* **24A** (2008)106.
[2] *Activity Report 2007* **25A** (2009) 114.
[3] *Activity Report 2008* **26A** (2010) 124.
[4] D. Teytelman, R. Akre, J.D. Fox, A. Krasnykh, C.H. Rivetta, D.Van Winkle, A. Drago, J.W. Flanagan, T. Naito, M. Tobiyama, *Proc. EPAC 2006* (2006) 3038.
[5] T. Nakamura, M. Masaki, K. Soutome, M. Takao, T. Hara, *Proc. PAC01* (2001) 1969.
[6] R. Takai, M. Tobiyama, J.W. Flanagan, T.M. Mitsuhashi, T. Obina, M. Tadano, *Proc. DIPAC09* (2009) 59.

2-4 Upgrade of Injection Control System

Since April 2009, the PF-ring has been operated with a top-up injection. Fluctuation in the stored current has been kept below 0.1% by switching the injection gate so that the output signal of the DC Current Transformer (DCCT) stays within the acceptable range. On the other hand, since the RF bucket into which the beam is injected is blindly selected without relation to the actual bunch current, the fluctuation in the bunch current over the bunch train tends to increase with the duration of top-up injection. This fluctuation should be minimized because it can cause not only unwanted heat generation of the ring components but also instabilities of the beam orbit [7]. In addition, our existing injection system cannot apply the top-up injection to any fill patterns except for the simple multibunch and single-bunch patterns; that is, we can never maintain the hybrid fill which has been tested as the new operation mode of the PF-ring [8]. To overcome these problems and make it possible to maintain arbitrary fill patterns with the top-up injection, a function to decide the next injection bucket based on information about the actual bunch current is required. We have developed a new injection control system with such a feedback function.

A block diagram of the new injection system is shown in Fig. 7. The heart of the system is a general-purpose oscilloscope ("Fill scope", Tektronix, DPO7104) connected across the output of a wall current monitor (WCM). In this oscilloscope, Microsoft Visual C++ [9] is installed as an integrated development environment, and an analytical program that can select out the bucket with the largest deviation from the nominal bunch current is running. This scope also functions as an EPICS-IOC [10] and immediately transfers the bucket address obtained from the analysis to the Linac control system via the network. This feedback process on the bunch current allows the top-up injection to be controlled so that the deviation between the actual and nominal bunch currents becomes small. The maximum repetition frequency of the bunch current feedback is around 25 Hz, which is faster than that of the beam injection. Although the analytical program is sufficiently stable over long time periods, for safety we wrote a script to monitor whether the program is alive or dead. Figure 8 is a comparison of the fill patterns (a) without and (b) with the bunch current feedback. The fluctuation in the bunch current over the bunch train has decreased from about 10% to less than 1%. As mentioned above, this improvement helps to stabilize the ring and beam conditions. The new injection system also enables us to generate and maintain arbitrary fill patterns including the hybrid fill. Figure 9 shows some examples of fill patterns generated with the new injection system. The configuration file to assign the desired pattern is loaded when the analytical program starts.

The new injection system has been used for user operation since March 2010 and has helped to smooth the multibunch fill. It also helps rapid recovery of the fill pattern after critical beam loss. Figure 10 shows fill patterns (a) before and (b) after recovery from beam loss caused by an injection kicker trouble. In the old system we had to re-inject the beam after dumping the stored beam, while in the new system, we can recover it in the minimum time by increasing just the injection frequency. We will continue to improve the system according to users' suggestions.

REFERENCES

[7] B. Kalantari, V. Schlott and T. Korhonen, *Proc. EPAC'04* (2004) 2882.
[8] *Photon Factory Activity Report 2008* **26A** (2010) 125.
[9] See, e.g., http://msdn.microsoft.com/.
[10] http://www.aps.anl.gov/epics/, and links therein.

Hardware
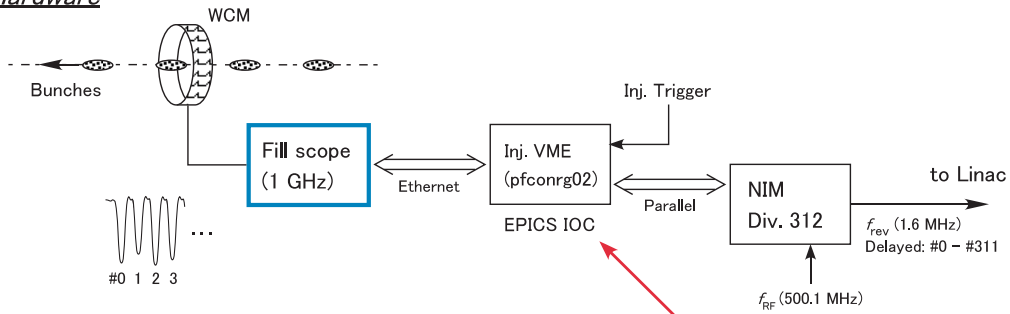
Software

Fill scope (Tektronix, DPO7104, 1 GHz, 20 GS/s)
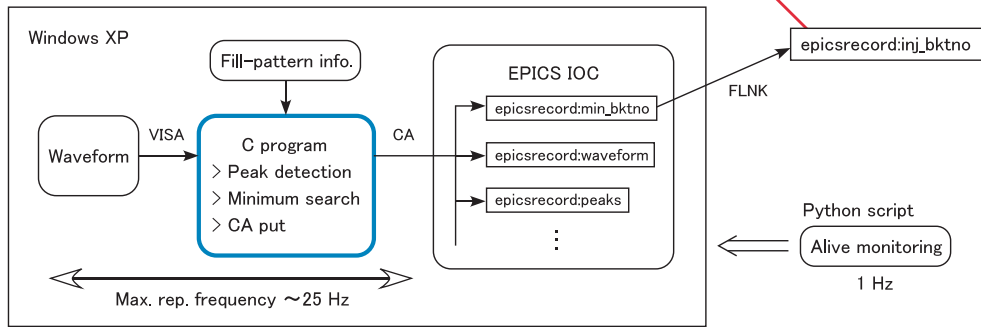
Figure 7
Block diagram of the new injection system.

(a) without feedback (b) with feedback
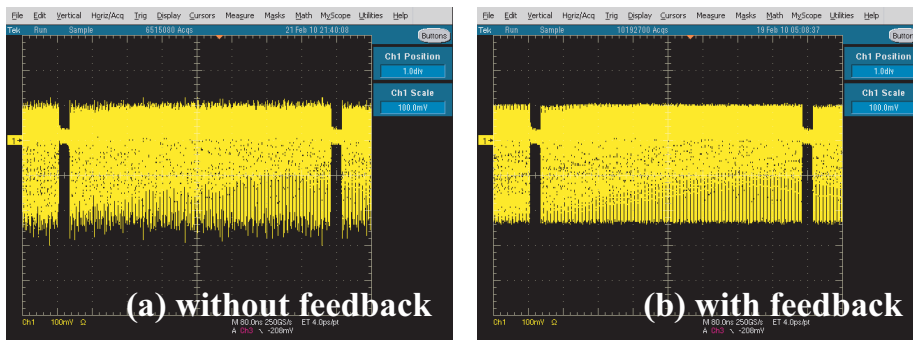
Figure 8
Fill patterns in the multibunch mode (300 bunches, 450 mA) obtained (a) without and (b) with the bunch current feedback.

comb linear

sinusoidal hybrid
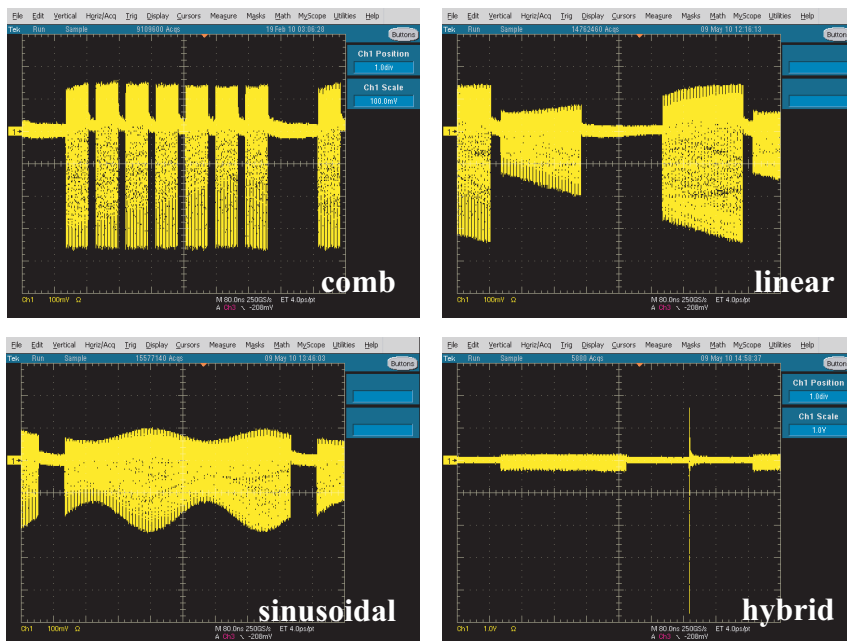
Figure 9
Examples of various fill patterns generated with the new injection system.
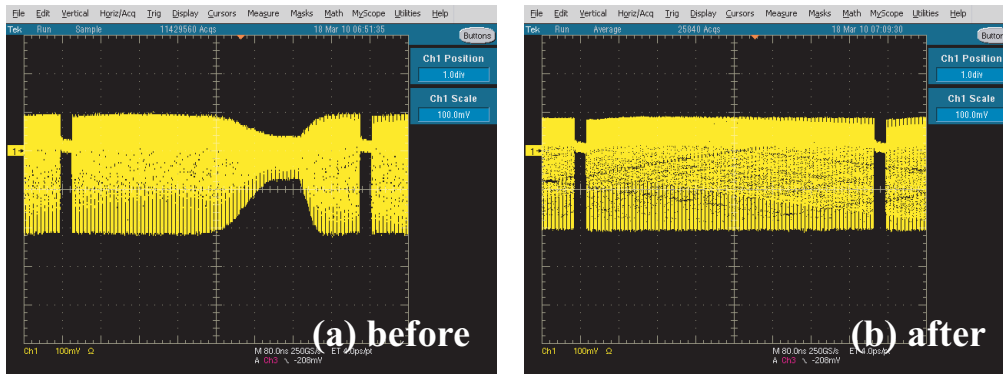
Figure 10
Recovery from critical beam loss. The original fill pattern is reproduced within five minutes from the start of recovery.

2-5 Status of the Fast Local Bump System

The fast local bump system for helicity switching is a good method for measuring the photon helicity-dependence of materials like circular and linear dichroism using a lock-in technique. In order to realize a fast local bump, five identical bump kickers were installed at a long straight section (B15-B16) of 8.9 m length at the PF ring in the spring of 2008. During 2008, we succeeded in orbit switching up to 0.1 Hz with orbit distortion smaller than 10% of the beam size outside of the bump (less than 30 μm in the horizontal direction and 5 μm in the vertical direction) and up to 70 Hz with larger orbit distortion. In order to improve the system and achieve 10-Hz operation, a new control system was introduced in 2009 as shown in Fig. 11. The new control system has four 2ch arbitrary function generators and one voltage-controlled 6ch attenuator module. Compared with the old control system, the waveforms are much smoother and the operations especially the beginning and ending of the switching, are much easier.

When we write the magnetic current for the ideal case as $I=A\sin(\omega t)$ and introduce the amplitude error ΔA and phase error $\Delta\varphi$, we obtain $I=(A+\Delta A)sin(\omega t+\Delta\varphi)$. Expanding the equation by small error terms and taking the linear part gives:

$$\Delta I = \Delta A\sin(\omega t) + A\Delta\varphi\cos(\omega t).$$

The amplitude errors generate beam oscillations that have the same phase as the bump itself, whereas the disturbances from the phase errors have a phase difference of 90 degrees. In the new correction method, we measure the beam oscillation outside of the bump with the phase information, distinguish the phase errors from the amplitude errors, and finally correct both errors respectively. Figure 12 shows the beam oscillations outside of the bump after correction for 10-Hz switching without the effect of the insertion device. Considering the measurement error, the orbit distortions are smaller than 10% of the beam size.

For the next step, in order to suppress the effects of the insertion device and make precise orbit corrections, an additional correction system with steering magnets will be installed.
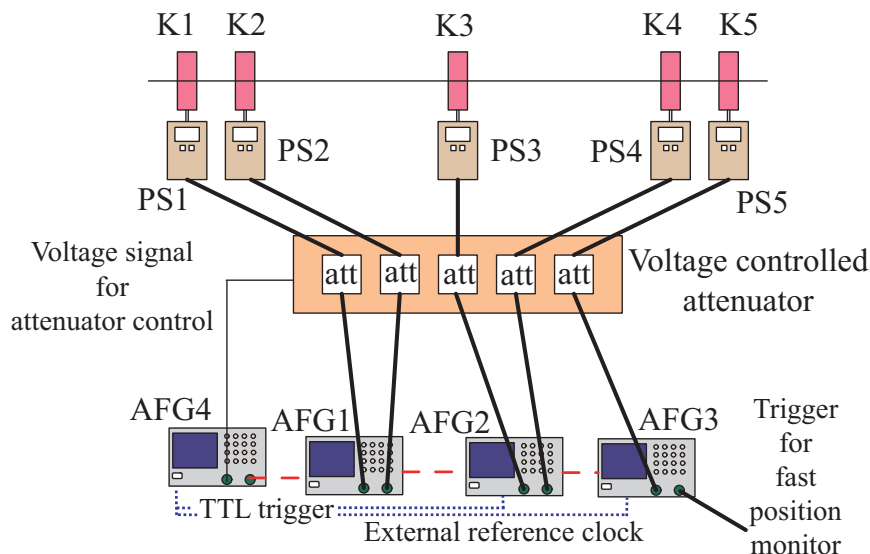
Figure 11
New control system.
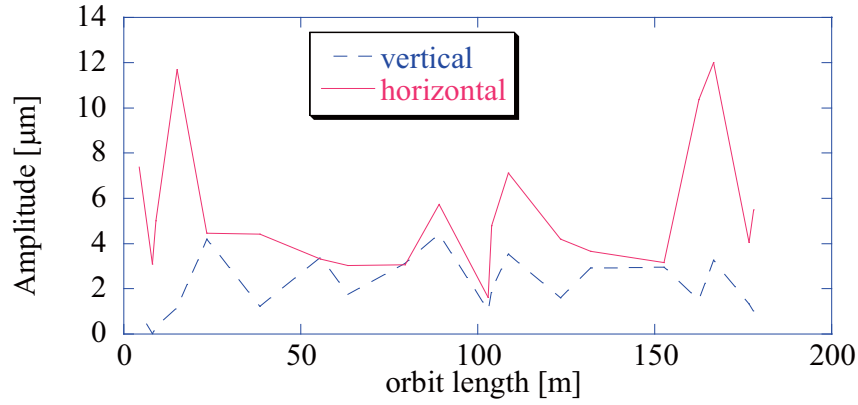
Figure 12
Orbit distortion of 10-Hz switching after tuning without insertion device effect.

2-6 Tune Shift Compensation for U#16-1

ID161 has two parameters, ϕ and ρ, as shown in Fig. 13. The polarization of photons can be changed by ϕ, and the energy by ρ. The gap between the magnetic poles of ID161 usually has a fixed value of 21 mm through the user run. The range of variation of ϕ and ρ for each mode for user operation are shown in Fig. 14.

The magnetic field of the insertion device generates the betatron tune shift of the electron beam. When the betatron tune is moved largely from the original operating point, for example, excitation of beam instability and deterioration of injection rate may occur. Therefore we correct the tune shift by using quadrupole magnets at both sides of straight section as shown in Fig. 15.

From the measurement results of the tune shift due to ID161 shown in Figure 16, the vertical tune shift is almost negligible. On the other hand, the horizontal tune shift is so large that correction is required. The horizontal tune shift $\Delta\nu_x [kHz]$ can be written by single polynomial equation of f [mm] and r [mm] as

$$\Delta\nu_x = c_1\rho + \left(f_1\left(\frac{\phi}{2}\right)^4 + f_2\left(\frac{\phi}{2}\right)^3 + f_3\left(\frac{\phi}{2}\right)^2 + f_4\left(\frac{\phi}{2}\right) \right)$$
$$\times \left(g_1\left(\frac{\rho}{2}\right)^3 + g_2\left(\frac{\rho}{2}\right)^2 + g_3\left(\frac{\rho}{2}\right) + g_4 \right)$$

From the response matrix of the tune shift for the correction coils of the quadrupole magnets, the required correction current $\Delta IQ_1 [A]$ and $\Delta IQ_2 [A]$ can be calculated by

$$\begin{pmatrix} \Delta I_{Q_1} \\ \Delta I_{Q_2} \end{pmatrix} = -\begin{pmatrix} R_{11} & R_{12} \\ R_{21} & R_{22} \end{pmatrix}\begin{pmatrix} \Delta\nu_x \\ \Delta\nu_y = 0 \end{pmatrix}$$
$$= -\begin{pmatrix} R_{11}\Delta\nu_x \\ R_{21}\Delta\nu_x \end{pmatrix}.$$

All coefficients are shown in Table 2. The maximum tune shift is about 0.01 (7 kHz) for $\rho/2 = \varphi/2 = 14mm$ without correction and the maximum required correction current is about 1.5 A. After the correction, the maximum tune shift is suppressed to less than 0.001 (2 kHz) for all modes.

(a) ρ

(b) ϕ
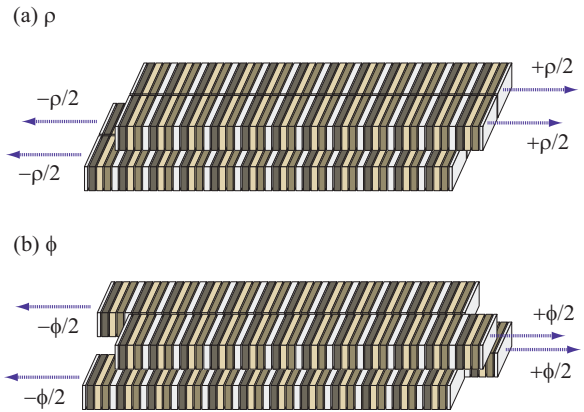
Figure 13
Two parameters, ρ and ϕ.
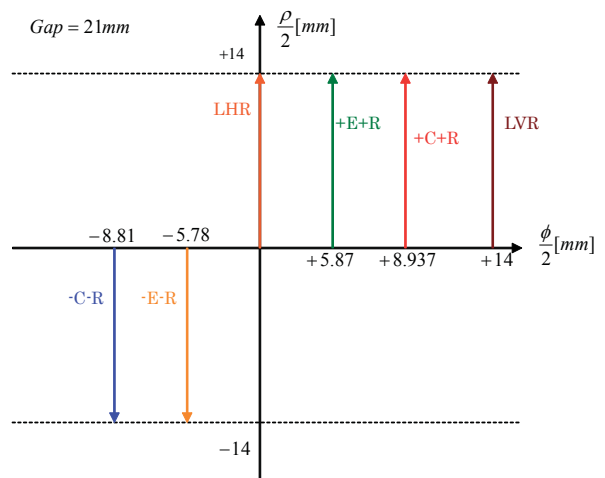
Figure 14
Variation of ρ and ϕ for each operation mode.
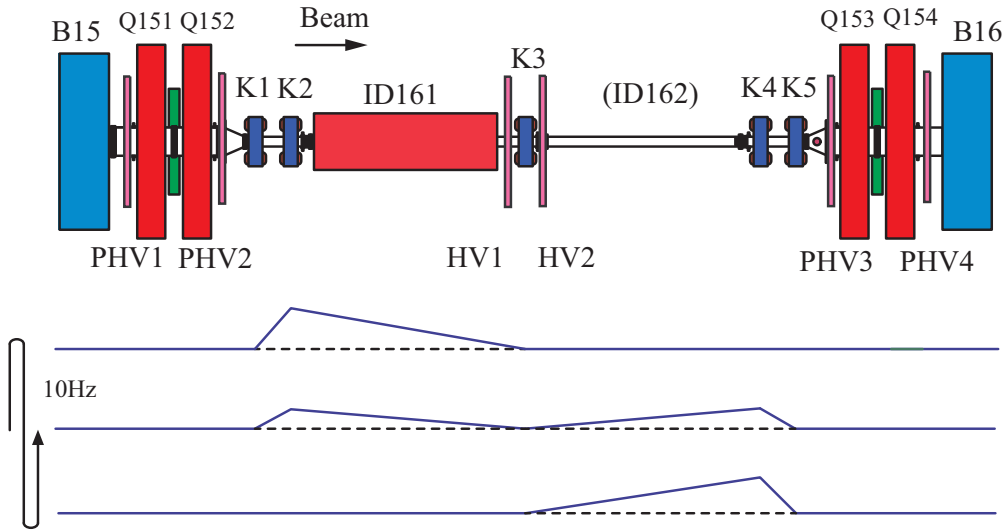
Figure 15
Magnet system for U16.
K1-5 are the bump kickers for fast orbit switching PHV1-4 the fast steering magnets for orbit switching and HV1 and 2 the slow steering magnets for photon axis adjustment. The correction coils attached on Q151-154 are used for the compensation of betatron tune shift.

(a) v_x: Measured horizontal tune
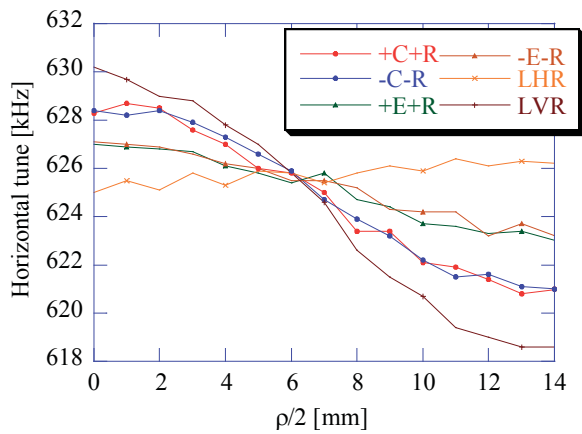
(b) v_x: Measured vertical tune
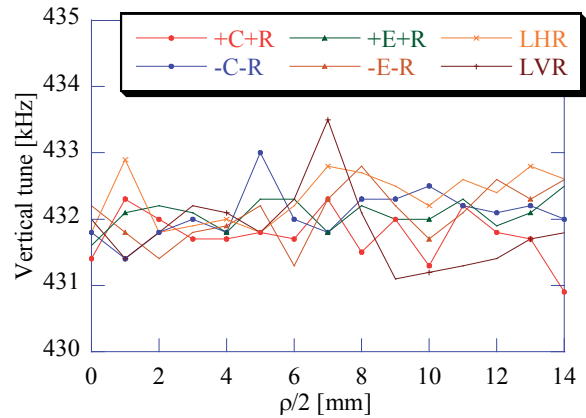
Figure 16
Measurement results of tune shifts.

Table 2 Coefficients.

c_1	8.01429E-02	g_1	1.43028E-04
f_1	-1.90011E-03	g_2	-3.08117E-03
f_2	5.72899E-04	g_3	-8.88958E-04
f_3	6.60000E-01	g_4	8.29787E-02
f_4	-4.08294E-02		
R_{11}	0.12220	R_{12}	-0.03061
R_{13}	0.06479	R_{14}	-0.08412

2-7 Construction and Operation of a New Short Gap Undulator(SGU#01)

After the reconstruction to upgrade of the PF storage ring, four 1.4m-long straight sections have been created for short gap undulators (SGU) with a period length of less than 20 mm. We constructed two SGUs (SUU#17 with a period length of 16 mm and SGU#03 with 18 mm) in an in-vacuum configuration for the X-ray light source with energy around 10 keV. The minimum gaps are both 4 mm and the operation of these SGUs is stable under the top-up operation of the PF ring.

SGU#01 is the third SGU with a period length of 12 mm. SGU#01 can produce photons of 12 keV at the third harmonic in the 2.5-GeV PF ring. The number of periods of SGU#01 is 39 and the maximum value of the deflection parameter is 0.78. As a magnet material, we
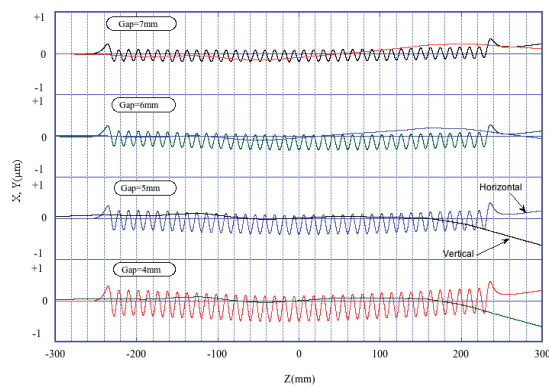
Figure 17
The calculated electron orbits are shown for several typical gaps. The magnetic adjustment was performed at the minimum gap of 4 mm.
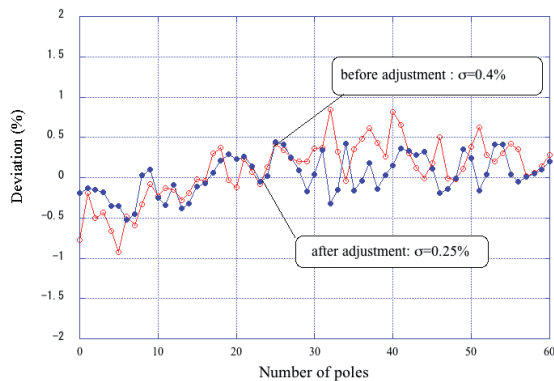
Figure 18
Distribution of the first integrals of the magnetic field at individual magnetic poles.

Figure 19
Photograph of SGU#01. SGU#01 (installed in the PF ring in September, 2009).

selected Nd-Fe-B alloy with remanent field of Br = 12kG and coercivity of iHC = 28kOe (NEOMAX35VH). These magnetic blocks are coated with TiN(5mm thick) for vacuum sealing.

The magnetic field was adjusted and the vacuum system of SGU#01 was commissioned using the same procedure that was developed for construction of the former SGUs.

The results of the magnetic field adjustment of SGU#01 are summarized in Fig. 17 and Fig. 18. Figure 17 shows the electron orbits at several typical

gaps and Fig. 18 shows the measured distributions of the first integrals of the magnetic field at individual magnetic poles after adjustment.

We installed SGU#01 in the PF ring in September, 2009. Figure 19 shows a photograph of SGU#01. Following commissioning study, user operation was started steadily. The minimum operation gap is 4 mm.

2-8 Magnetic Field Adjustment of Polarizing Undulator (U#16-2)

At the 2.5-GeV Photon Factory (PF) storage ring, we have been developing a rapid-polarization-switching source in the VUV and soft X-ray region to be installed in the straight section between bending magnets B15 and B16 in the PF ring. The source consists of two tandem APPLE-II-type elliptically polarizing undulators (EPU), namely U#16-1 and U#16-2, and a fast kicker system. These two EPUs are designed to obtain soft x-rays in the energy region from 200 eV to 1 keV under various polarization states. We constructed U#16-1 and installed it in the PF ring in March 2008. Operation of U#16-1 for user experiments has been ongoing since April 2008. U#16-1 became operational for user experiments after commissioning in the PF ring. Experiments using circular polarization have been conducted successfully since May 2008. Currently, the available polarization modes are circular polarization (Bx/By = 1), elliptical polarization (Bx/By = 1/2), and linear polarization in the horizontal and vertical directions.

As the next step, we are constructing a second EPU, U#16-2. The magnetic adjustment of U#16-2 was finished as scheduled. Figure 20 shows a photograph of U#16-2 during the magnetic adjustment. We developed a procedure for optimizing the arrangement of magnetic arrays of U#16-2 as described below. By adopting a pure Halbach magnet arrangement, we can estimate the property of the total magnetic field distribution of the EPU by superposing of individual fields of each of the magnets that make up the EPU. First, we measured the magnetic field distribution of each magnet block. Second, we determined the suitable arrangement of the magnetic arrays by a simulated annealing method using the measured field data of the magnets. Finally, we analyzed the results of the superposed magnetic field distribution at the calculated arrangement of the magnets in a planar undulator mode.

After we assembled the magnet blocks using the simulated arrangement, we measured the magnetic field distribution of U#16-2 in the planar undulator mode with the original position of the four rows at a minimum gap of 21 mm. The standard deviation of the phase errors was only 1.5 degrees at the first measurement without any adjustment. This shows that the method we used to determine the magnetic arrangement works
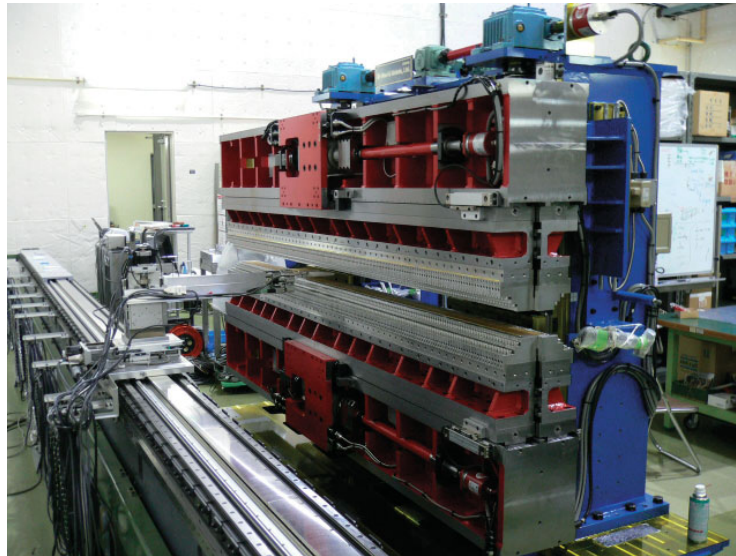
Figure 20
Phtograph of U#16-2 during the magnetic measurement.
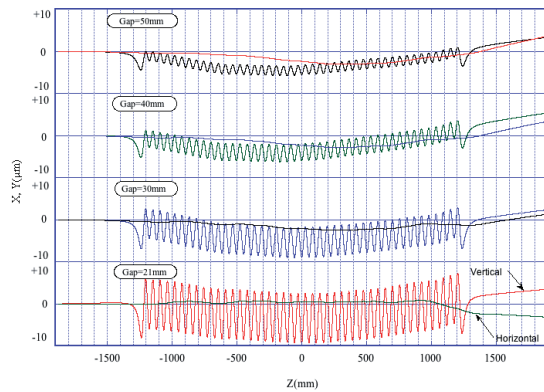
Figure 21
The electron orbits are shown at several typical gaps. The electron orbits are calculated based on measured data in the planar undulator mode.
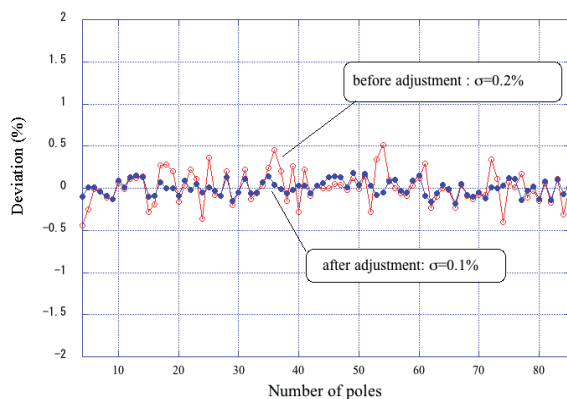
Figure 22
The distribution of the first integrals of the magnetic field at individual magnetic poles. We adjusted the horizontal position of the magnetic blocks using shims to improve the distribution of the first integrals of the magnetic field at individual magnetic poles.

well, and all the magnet blocks were arranged precisely on the magnet-mounting beams of the EPU.

For the distribution of the first integrals of the magnetic field at individual magnetic poles, we adjusted the horizontal position of the magnetic blocks using shims. The results of the magnetic field adjustment of U#16-2 are summarized in Fig. 21 and Fig. 22. Figure 21 shows the electron orbits at several typical gaps, which were calculated based on measured data in the planar undulator mode. The measured distributions of the first integrals of the magnetic field at individual magnetic poles after adjustment are compared with those before adjustment in Fig. 22.

After the magnetic field adjustment, we will continue magnetic measurements of U#16-2 under various conditions of all operation modes. After the magnetic measurements, we will install U#16-2 in the PF ring this summer.

2-9 The New Control System of EMPW#28

EMPW#28 was constructed originally as an elliptical multi-pole wiggler in the PF ring in 1989. Recently, EMPW#28 has been mainly used as a source of circular polarized photons below 500 eV since the reconstruction of BL28. The gap and the magnetic row of EMPW#28 have been driven by the AC servo motor system which was built at the same time as EMPW#28. With this old system, we managed to perform COD correction for the change in gap for independent tuning. However, we could not control COD correction during the change in polarization state of EMPW#28 by moving

magnetic rows. Since the influence of the orbit fluctuation was serious for user experiments, the change of polarization state of EMPW#28 was restricted to once per day.

We have renewed the AC servo motor drivers and the gap controller for EMPW#28. The new control system of EMPW#28 was developed with EPICS and operation started stably in October 2009. A study for the correcting of the orbit fluctuations during polarization switching of EMPW#28 was carried out step by step using steering magnets located at both ends of the ID. The orbit fluctuations were measured by using the BPM system for both the vertical and horizontal directions. The total number of BPMs was 64. Figures 23 and Fig. 24 show the results of the orbit fluctuations as a function of the BPM number during circular polarization switching with and without the corrections. The orbit fluctuations after the correction were reduced to less than 10 mm around the ring in both directions. The operation of polarization switching for EMPW#28 was begun in April 2010. The user can change the gap and the polarization mode of EMPW#28 at any time during operation.
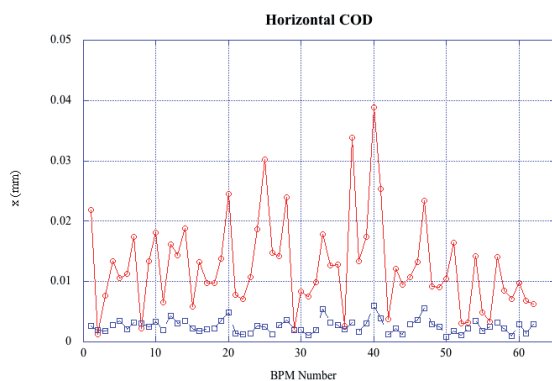
Figure 23
Comparison of horizontal orbit fluctuations. The absolute values of the displacement are shown at every BPM in the PF ring. The red circles show the case without correction and the blue squares show the case with correction.
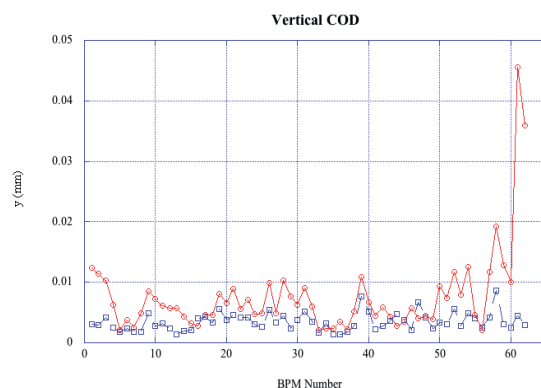
Figure 24
Comparison of vertical orbit fluctuations.

2-10 Beamline Front-End for In-Vacuum Short Gap Undulators

Beamline Front-end for In-Vacuum Short Gap Undulators

The straight-section upgrade project of the PF created four new short straight sections capable of housing in-vacuum short gap undulators [11]. The first to third short gap undulators SGU#17, SGU#03 and SGU#01 were installed at the PF storage ring in 2005, 2006 and 2009, respectively [12]. The beamline front-ends for these short gap undulators are described in this article.

The power density at the front-end is nearly equal to that of the multi-pole wiggler (MPW) radiation, because the beam size of the undulator radiation is smaller and the source point of the short gap undulator is nearer to the front-ends. To accommodate this situation, a new beamline front-end was designed that is capable of handling the power of the short gap undulators. The photon shutter was re-designed. The front-end components had to be set up very precisely because of the small beam size for the short gap undulator radiation [13, 14].

Design Concept of the New BL-17 Front-end

Figure 25 is the side view of the new BL-17 front-end showing its layout and the major components. To shorten the total length of the front-end, (1) we removed the fast closing valve (FCV) and the acoustic delay line (ADL), and instead, we made every aperture as small as possible with a vacuum-tight structure, (2) we changed the material of the safety shutter block from 400 mm-thick stainless steel to 250 mm-thick tungsten.

A safety shutter, made of a tungsten block 100 mm in width x 50 mm in height x 250 mm in thickness, was installed to protect personnel from radiation. A water-cooled photon shutter protects the safety shutter and valves from direct irradiation by the undulator radiation. A system composed of a fixed mask, graphite filter and Be windows was directly connected to the downstream end of the front-end.

Design Concept of the New BL-3 Front-End

The front-end of the two bending magnets B02 and B03 of beamline BL-3 was partially reconstructed in response to installation of the short gap undulator SGU#03. Figure 26(a) is a schematic layout of the new BL-3 front-end showing its layout and the major components. Figure 26(b) is a horizontal optical path diagram of the BL-3 front-end schematically showing that horizontal acceptance is 4 mrad for the old branch A, 1 mrad for the new branch A, 10 mrad for the branch B, and 2 mrad for the branch C.

The new BL-3 has three branch beamlines. The new BL-3A is the undulator SGU#03 radiation branch beamline, and the BL-3B and BL-3C are the bending magnet B03 radiation branch beamlines. Before the SGU#03 was installed, the old BL-3A was the branch beamline
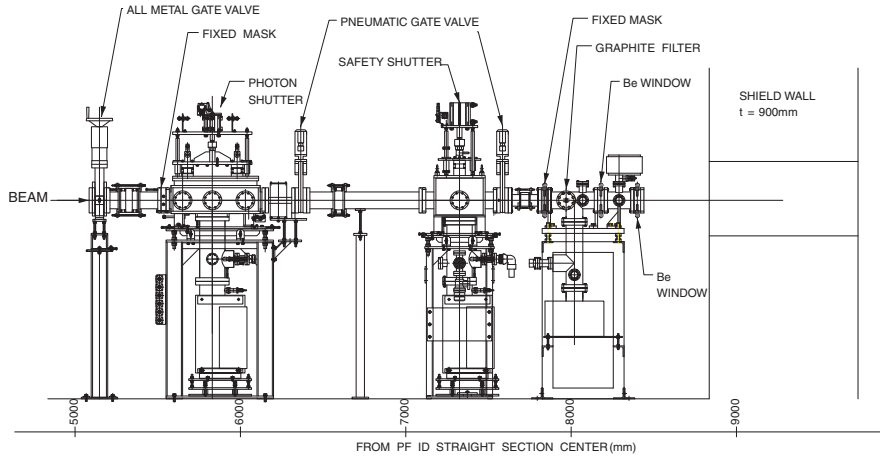
Figure 25
Component layout of the new BL-17 front-end.
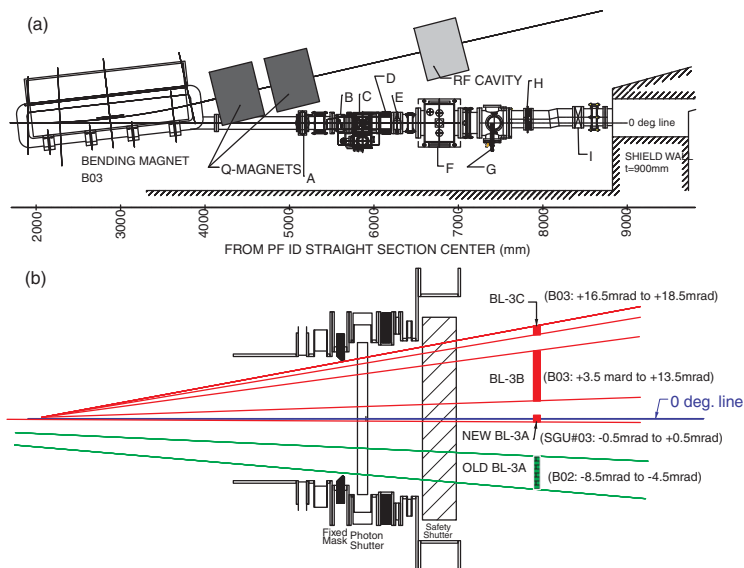
Figure 26
(a) Plan view of the new BL-3 front-end for the short gap undulator SGU#03 and bending magnet B03 radiation. Labeled components are: A) all-metal gate valve; B) tapering fixed mask; C) photon shutter; D) Pb shield for viton seal of downstream gate valve; E) pneumatic gate valve; F) safety shutter; G) photon absorber for radiation from bending magnet B02; H) fixed mask with three holes; I) pneumatic gate valve.
(b) Horizontal optical path diagram of the BL-3 front-end.
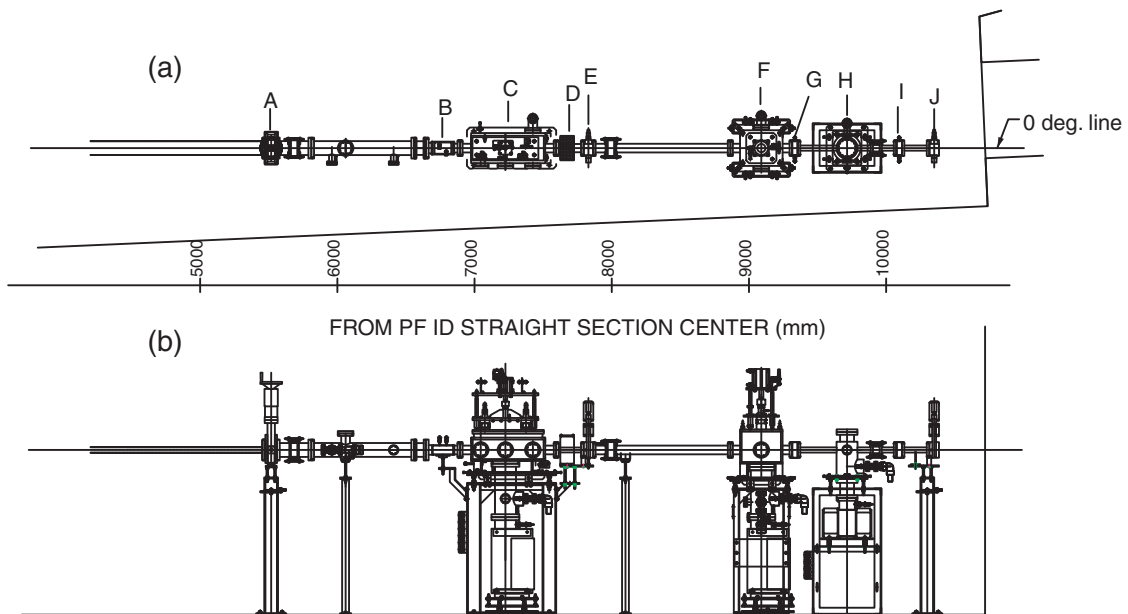
Figure 27
(a) Plan view of the new BL-1 front-end for undulator SGU#01 radiation. Labeled components are: A) all-metal gate valve; B) tapering fixed mask; C) photon shutter; D) Pb shield for viton seal of downstream gate valve; E) pneumatic gate valve; F) safety shutter; G) fixed mask; H) vacuum buffer chamber; I) fixed mask; J) pneumatic gate valve.
(b) Elevation view of the new BL-1 front-end.

for the bending magnet B02 radiation. Because the RF cavity had been close to the BL-3 front-end, the BL-3 front-end had to be set along the zero degree line and the old BL-3 front-end was for the bending magnets B02 and B03 radiation. At the time of installing the SGU#03, we partially changed the BL-3 front-end downstream components below the safety shutter. To cut the bending magnet B02 radiation, we set a water-cooled copper rod as a photon absorber for B02 radiation (Fig. 26 labeled "G"). To separate the undulator SGU#03 radiation (BL-3A) and the bending magnet B03 radiation (BL-3B and BL-3C), we set a water-cooled copper fixed mask with three holes (Fig. 26 labeled "H").

Design Concept of the New BL-1 Front-end

The front-end of beamline BL-1 was totally reconstructed in response to installation of the short gap undulator SGU#01. Figure 3 is a schematic layout of the new BL-1 front-end for the undulator SGU#01 radiation showing its layout and the major components. The old BL-1 front-end was for the bending magnet B01 radiation and the front-end was set along the 2.5-degree line. At the time of installing the SGU#01, we removed all of the old BL-1 front-end and set the new BL-1 front-end components along the zero degree line. The new BL-1 components had to be compact, because the shield wall around BL-1 is designed for a front-end along the 2.5-degree line and the downstream part of the new BL-1 front-end is very close to the side of the shield wall (Fig. 27(a)). The two water-cooled fixed masks (Fig. 27, labeled "G" and "I") and the vacuum buffer chamber with an ion pump (Fig. 27, labeled "H") are used for differential pumping in order to keep ultra high vacuum (UHV) in the BL-1 front-end.

REFERENCES
[11] T. Honda, S. Asaoka, W. X. Cheng, K. Haga, K. Harada, Y. Hori, M. Izawa, T. Kasuga, Y. Kobayashi, H. Maezawa, A. Mishina, T. Mitsuhashi, T. Miyajima, H. Miyauchi, S. Nagahashi, T. Nogami, T. Obina, C. O. Pak, S. Sakanaka, H. Sasaki, Y. Sato, T. Shioya, M. Tadano, T. Takahashi, Y. Tanimoto, K. Tsuchiya, T. Uchiyama, A. Ueda, K. Umemori and S. Yamamoto, *AIP Conf. Proc.* **879** (2007) 87.
[12] S. Yamamoto, K. Tsuchiya, H. Sasaki, T. Aoto and T. Shioya, *AIP Conf. Proc.* **1234** (2010) 599.
[13] H. Miyauchi, S. Asaoka and H. Maezawa, *AIP Conf. Proc.* **879** (2007) 1038.
[14] H. Miyauchi, T. Tahara and S. Asaoka, *AIP Conf. Proc.* **1234** (2010) 713.

2-11 New Power Supply for the Pulsed Sextuple Magnet

New power supply for the pulsed sextuple magnet

We successfully demonstrated the new injection scheme using a pulsed sextupole magnet (PSM) at the Photon Factory storage ring (PF-ring) in 2008 [15].

The sextupole magnetic flux density is given by $= a(x^2 - y^2)$. Therefore, on the y = 0 plane, an electron beam is deflected in proportion to the square of the distance from the magnetic center. In this new injection scheme, we use this property of the sextupole magnet to inject an electron beam and to suppress stored beam oscillation during beam injection. A stored beam that passes through approximately the center of the magnet feels very low field but an injection beam that passes at a distance of 15 mm from the center of the magnet at the PSM is deflected and enters the stable area for storage.

When we demonstrated the PSM injection, we used the power supply for the pulsed quadruple magnet (PQM) that was installed in the PF-Advance ring [16]. The pulse width of this power supply is 2.4 μsec, and the injection beam is deflected two times (2-turn injection) at the PF-ring which has a revolution period of 624 nsec. We estimated the effect of the second kick, and found that 2-turn injection has about a 30% lower injection rate than 1-turn injection. The PQM uses an old second-hand DC power supply made about 30 years ago, so we consider the PQM power supply is not suitable for practical use.

As the next step, we developed a new power supply aiming to start practical use of the PSM in 2009. A photograph of the new power supply with its cover opened to reveal the main circuit is shown in Fig. 28. A block diagram of the circuit is shown in Fig. 29, in which electrical elements are drawn in almost the same positions as in the real power supply (see Fig. 28).

The current pulse is made as follows. At first, the capacitor is charged by DC power supply, and then the thyratron, which is a high peak power electrical switch, is turned on by an external trigger. A current pulse then flows in the PSM, which is an inductive element.

We designed the new power supply with a pulse width of 1.2 μsec, peak current of 3000 A, maximum voltage of under 30 kV, and maximum repetition rate of 25 pulses per second. This circuit is mainly an LC circuit. The PSM has inductance of 2.4 μH at 100 kHz, so to achieve a pulse width of 1.2 μsec under 30 kV, the power supply inductance must be less than 1.4 μH. We designed the main circuit as a coaxial structure to create a low-inductance power supply. The thyratron, diode, and adjustment capacitor are covered by a shield box, and the connector to the PSM is a coaxial structure (see Fig. 28). The inductance of the power supply is 1.29 μH estimated from the pulse width and capacitance.

Figure 30 shows the output waveform of the new power supply. It is a half-sine wave and a rather large undershoot continues after the main wave. A multi-gap thyratron has a long recovery time; the recovery time of the E2V CX1175C (2-gap thyratron) is over 50 μsec. Therefore, we used a high voltage diode (Origin Electronic MD50SH05K) to prevent the flow of reverse current. However, this diode has a maximum reverse re-

covery time (trr) of 0.5 msec, and reverse current flows in the circuit during this 0.5 μsec, causing the large undershoot.

However, this undershoot is harmless, because the revolution period is 624 nsec at the PF-ring; when we adjust the first turn of the injection beam on the top of the pulse wave, the second turn is the zero-cross point of the wave and the third turn is after the undershoot.

REFERENCES

[15] H. Takaki, N. Nakamura, Y. Kobayashi, K. Harada, T. Miyajima, A. Ueda, S. Nagahashi, M. Shimada, T. Obina, T. Honda, *Phys. Rev. ST Accel. Beams* **13** (2010)020705.
[16] K. Harada, Y. Kobahashi, T. Miyajima, S. Nagahashi, *Phys. Rev. ST Accel. Beams* **10** (2007) 123501.
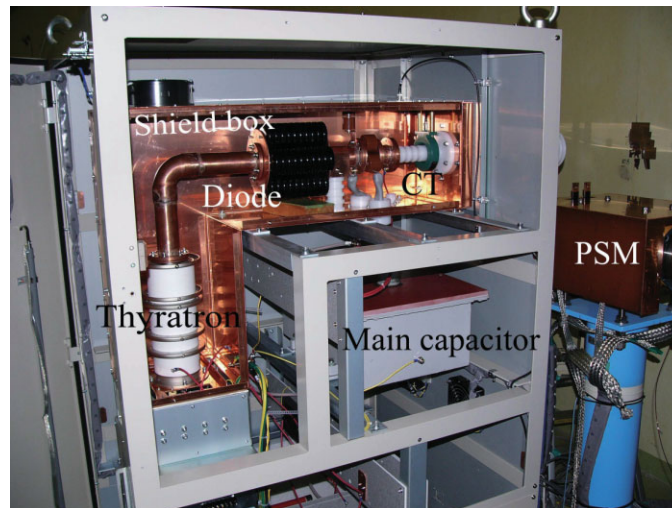
Figure 28
PSM power supply. The covers are opened to reveal the inner main circuit.
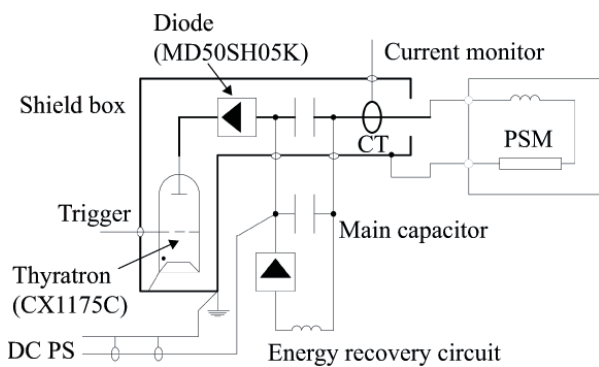
Figure 29
Block diagram of the circuit. The electrical elements are drawn in almost the same positions in the real power supply.
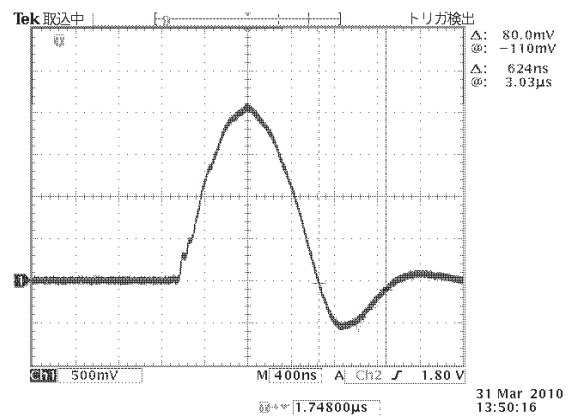
Figure 30
Typical current waveform of the PSM power supply.